

Combined tomographic forward and inverse modeling of active seismic refraction profiling data

5

Ivan Koulakov (1) and Heidrun Kopp (2)

10

(1) Institute of Petroleum Geology and Geophysics, SB RAS,
Prospekt Akademika Koptuga, 3, Novosibirsk, 630090, Russia

e-mail: KoulakovIY@ipgg.nsc.ru

Phone: +7 383 3309201

15

(2) IFM-GEOMAR, Leibniz Institute of Marine Sciences

Wischhofstr. 1-3, 24148 Kiel, Germany

e-mail: hkopp@ifm-geomar.de

Phone: +49 431 6002334

20

For submission to JGR Solid Earth

25

Novosibirsk - Kiel, May 2008

30 Abstract

We present a new code for combined forward and inverse tomographic modeling based on first-arrival travel times of active seismic refraction profiling data (*PROFIT* – Profile Forward and Inverse Tomographic modeling). The main features of the algorithm involve the original version of bending ray tracing, parameterization based on nodes, variable grid size definition determined
35 by the ray density, and regularization of the inversion. The key purpose of applying the *PROFIT* code is rather not in solely producing the tomographic image of a continuous velocity field, but in creating a geologically reasonable synthetic model. This model then includes first-order velocity changes representing petrophysical boundaries and is thus better suited for a geological-tectonic interpretation than its smoothed tomographic counterpart. After performing forward and
40 inverse modeling, the synthetic model will reproduce a congeneric model to the tomographic inversion result of the observed data. We demonstrate the working ability of the code using two marine datasets acquired in the Musicians Seamount Province (Pacific Ocean). The results of the tomographic inversion clearly resolve the dominating extrusive volcanism. In addition, the combined forward and inverse approach tests a large variety of synthetic models to fit the
45 observed data tomography. Along both profiles, the preferred structural model includes a strong positive velocity anomaly extending into the seamount edifice. We suggest that this anomaly pattern represents secondary intrusive processes, which are only revealed by the combined tomographic forward and inverse modeling and could not be resolved by exclusively applying a tomographic inversion.

50

Key words: seismic profiling, tomography, forward modeling, synthetic model, hot-spot ridge interaction

1. Introduction

55 The main purpose of this paper is to present a new code for combined forward and inverse tomographic modeling based on active seismic refraction profiling data (*PROFIT* – PROfile Forward and Inverse Tomographic modeling). The code may be used to determine the isotropic seismic velocity distribution along 2D-profiles.

60 The amount of high-quality seismic data acquired in a variety of different geologic-tectonic settings has risen tremendously over the past decades. The increased data density along seismic profiles progressively requires an automatization of processing and interpretation tools. The interpretation results then provide rich information about the structure of the crust and the uppermost mantle. Kinematic modeling schemes based on the travel time information provided by refracted seismic rays represent the dominant approach to wide-angle data modeling. A
65 practical realization and coevally provided possibilities for an unbiased verification of the results is still of imminent importance in refraction seismics. All commonly used approaches have some advantages as well as shortcomings.

 There are two basic schemes for modeling refraction data: forward modeling and tomographic inversion, which are usually performed independently of each other. Forward
70 modeling aims at obtaining a velocity model, which provides the best fit to the observed travel times (e. g. [Luetgert, 1992](#); [Zelt and Smith, 1992](#)). Forward modeling is usually performed manually and strongly depends on the experience of the scientist. In many cases, the comparison of travel times provides an ambiguous and non-unique solution. It is fairly difficult to formalize and render automatic this process. Therefore, it becomes more and more popular to use the
75 alternative approach of tomographic inversion, which seems to be less dependent on the subjective input of the user. During the last decades, several different tomographic approaches were actively developed for the purposes of non-commercial active source profiling (e.g. [Hole, 1992](#); [Zelt and Barton, 1998](#); [Korenaga et al., 2000](#); [Hobro et al., 2003](#)). There are some codes, which are based on first arrival data whereas others also employ later phases. A number of codes
80 allow using inhomogeneous starting models based on existing a-priori information.

 However, the tomographic approach has some obvious limitations, which make the interpretation of the results quite intricate. First of all, in most cases, the tomography results provide a continuous velocity-depth distribution without first-order velocity contrasts. Given a starting model with pre-defined velocity interfaces, these cannot be shifted by the obtained
85 relative velocity anomalies during the tomographic inversion. In most applied studies, the output of the tomographic inversion is a continuous velocity model, which is presented by contour lines. At the same time, however, it is a common practice to base the geologic-tectonic interpretation on the distribution of the main petrophysical interfaces (e.g., basement, Moho), which seem to

follow some contour lines (e.g., 6.0 km/s, 7.8 km/s). This is an obvious contradiction, which
90 must be considered as the main shortcoming of the tomographic approach in the wide-angle
schemes.

In many cases, it is useful to predefine the starting model based on a-priori information of
the local study area. However, the final solution would mostly be controlled by this pre-
definition of the starting model. As a consequence, it will be difficult to judge if any similarities
95 between the input model and the final output model are an adequate representation of the natural
setting. Just analyzing the root-mean-square values (RMS) of travel-time residuals after the
inversion might not be sufficient. For some parts of the study area the solution may be well
founded, resulting in small average RMS values, whereas other parts of the model (especially
areas with a sparse ray coverage) may not be authentic. Another problem of tomography is that,
100 in case of non-sufficient ray coverage, the solution can contain some artifacts, which are usually
not easily separated from relevant patterns.

We propose a new approach, which combines forward modeling and tomographic
inversion to solve some of the above mentioned issues. Here we present a newly-developed code
(*PROFIT* – Profile Forward and Inverse Tomographic modeling) for combined tomographic
105 inversion and forward modeling which can be applied for modeling of both marine and land
active seismic profiling data. Regularized inversions commonly have high computation and
memory requirements (Zelt and Barton, 1998). One of the main advantages of the new code is its
high calculation speed with respect to its existing analogues. The code allows user-friendly
creation of complex seismic models as input for subsequent forward and inverse modeling.

110 In this paper, the code is demonstrated using a real dataset of two seismic marine profiles
in the Musicians Seamount Province located north of the Hawaiian Chain (Pacific Ocean). The
data processing is described in detail in Kopp et al., 2003. The inactive Musicians Seamounts
form coherent volcanic elongated ridges (VERs), which originated from hot spot-ridge
interaction. Their evolution is related to off-axis volcanism on top of partially melting
115 asthenospheric flow channels linking the Euterpe Hotspot and the Pacific-Farallon spreading
center. The previously conducted tomographic inversion could clearly resolve the extrusive style
of volcanism of the Musicians Seamounts, which is manifested in the crustal thickening of
oceanic layer 2. This data set was chosen because the coherent and uniform phase distribution in
the seismic sections is favorable for testing a new code. At the same time, the presented
120 approach has also been applied in investigations of the subduction zone along two profiles
offshore central Java (paper in preparation) and other areas, which represent complicated
tectonic-geologic settings.

2. Algorithm for tomographic inversion

125 2.1. General notes

The *PROFIT* code consists of two major components. The first part comprises the tomographic inversion tools and is described in this section. This part can be used as an independent and separate tomographic code for processing seismic refraction data. The second part of the *PROFIT* code is geared towards combined forward and inverse modeling and is presented in Section 3.2 using an example of real observed data.

130 The *PROFIT* code is created using the *FORTRAN-90* programming language and is designed in *MS Windows OS* (alternatively, compilation for *LINUX* is possible). The code is user-friendly and simple in operating and optimizes computation time (for example an outdated laptop of 700 Mhz of CPU speed performs the inversion for ~2000 rays in 9 iterations including 135 2D ray tracing and inversion in each step in about 30 minutes). The description of the code and the executable version are available online on www.ivan-art.com/science/PROFIT.

The general structure of the algorithm for tomographic inversion within the *PROFIT* code is based on established schemes common for this type of investigation. The calculations are performed by iterative execution of the following steps:

- 140 1. Ray tracing in the 2D velocity model (starting model in 1st iteration, or updated velocity model after previous iterations);
2. Construction of the parameterization grid (only in 1st iteration);
3. Calculation of the matrix and inversion;
4. Updating the velocity model. Go to the step 1.

145

In the following, we will describe the most important features of each of these steps.

2.2. Ray tracing

The ray tracing used in this code is based on the Fermat principle and consists of finding 150 a path which provides the minimum travel time between source and receiver. This idea is the basis of the bending method of ray tracing (e.g. [Um & Thurber, 1987](#)), which has been widely applied for decades and evolved as a standard in different practical codes of local earthquake tomography (e.g. [Thurber, 1993](#)) and seismic modeling (e.g. [Korenaga et al., 2000](#)). We have created an alternative version of the bending algorithm, which is schematically shown in [Figure 1](#). Finding the path of minimum travel time consists of subsequent execution of several bending regimes. In the initial step ([Figure 1A](#)), the bounce point on the sea bottom (point *b*) is located just beneath the source *s*. We start from the straight line between the bounce point *b* and the receiver *r* and deform it to obtain the minimum travel time. In the first approximation, the

160 deviation A with respect to the initial straight path is computed according to the following formula:

$$A = B \cos\left(\pi \frac{s - D_{tot}/2}{D_{tot}}\right) \quad [1]$$

where B is the value of bending, s is the distance along the initial path, and D_{tot} is the length of the initial path. The value of B is adjusted to obtain the curve $\gamma(B)$ which provides the minimum value of the integral:

$$165 \quad t = \int_{\gamma(B)} \frac{ds}{V(s)} \quad [2]$$

where $V(s)$ is the velocity distribution along the ray.

In the second step (Figure 1B), we move the bounce point b along the sea bottom to obtain the minimum value of integral [2]. For land observations, this step will be omitted, because the location of s and b are identical.

170 At the next stage, further deviations of the path between b and r are performed iteratively using a formula for bending values:

$$A = \frac{B}{2} \cos\left(2\pi \frac{s - (S_2 - S_1)/2}{(S_2 - S_1)}\right) + \frac{1}{2} \quad [3]$$

where S_1 and S_2 correspond to the length along the path in the beginning and at the end of the current segment.

175 During the first iteration, the bending is performed for the entire segment $b-r$ in a similar way as demonstrated in Figure 1A, but using formula [3]. In the second iteration (Figure 1C), the path is divided into two segments of equal lengths ($b-m1$ and $m1-r$), and each of them is bended according to formula [3]. After determining the minimum time curve, the entire path is divided into three parts (Figure 1D), and the same approach of bending is performed for segments $b-m1$,
180 $m1-m2$, and $m2-r$. Subsequently, this procedure is repeated for the path divided into four, five and more parts. The bending terminates when the length of the sections becomes smaller than a predefined value.

2.3. Parameterization

185 We define the 2D velocity distribution using the node parameterization, which was previously developed for 3D tomographic inversion using the *LOTOS-07* code (Koulakov et al., 2007; Koulakov, 2008). The values of velocity anomalies are interpolated bilinearly between the nodes. The nodes are defined in a set of vertical lines with a fixed predefined spacing. Along each line we compute the values of the ray density (summary ray length in a unit volume). The
190 nodes then are distributed according to the ray density. To avoid excessive node fluctuations, we

define the minimal spacing between the nodes in the vertical direction. In areas with a lower ray density the distance between nodes is larger. We do not install the nodes in areas where the ray density is less than a predefined value (e.g. 0.1 of average value). It should be noted that for wide-angle observations, the node spacing in horizontal and vertical directions is not equivalent (e.g. 2 km and 0.3 km) as we expect a different vertical and horizontal resolution. **Figure 2** presents an example of node distributions according to the ray paths corresponding to seismic Profile 02 described later. Based on previous investigations (**Kopp et al., 2003**), the employed grid sizes are small enough to resolve the velocity anomalies expected in the study area (**Figure S2**). An evaluation of grid spacing is discussed in the supplementary material. The grid nodes are installed only in the first iteration according to the ray distribution traced in the starting model. During later iterations, velocity variations are updated based on the same nodes. By linking the node distribution to the ray density, the grid may specifically be adapted to any particular data set and accounts for the distinct variation in ray density. The ray distribution and density is a unique feature to every refraction study, depending on the instrument layout but also on the composition and geometry of the subsurface. This requires a non-uniform grid, with variable grid sizes dependant on the ray distribution and density.

2.4. Matrix calculation and inversion.

Calculation of the first derivative matrix is performed using the ray paths computed based on the ray tracing in the 2D model. Each element of the matrix, $A_{ij} = \partial t_i / \partial v_j$, is equal to the time deviation along the i -th ray due to a unit velocity perturbation in the j -th node. The elements of the matrix are computed numerically.

Inversion of the entire sparse A matrix is performed using an iterative *LSQR* algorithm (**Page, Saunders, 1982, Van der Sluis, van der Vorst, 1987**). Amplitude and smoothness of the solution is controlled by two additional blocks. The first block is a diagonal matrix with only one element in each line and zero in the data vector. Increasing the weight of this block causes a reduction of the amplitude of the derived velocity anomalies. The second block controls the smoothing of the solution. Each line of this block contains two equal nonzero elements of opposite signs, which correspond to all combinations of neighboring nodes in the parameterization grid. The data vector in this block is also zero. Increasing the weight of this block causes a reduction of the difference between solutions in neighboring nodes, which results in smoothing of the computed velocity fields.

The optimum values of these parameters depend on several factors. For example, when increasing the data amount, the damping parameters should be increased, while in the case of increasing the numbers of nodes due to smaller spacing, the damping should be decreased. In the

case of larger noise level in the data, damping should be stronger to keep the solution stable. The process of finding the damping coefficients is not formalized yet. The relationships between the number of parameters, rays and values of amplitude and smoothing coefficients are not linear. For example, when the number of rays doubles, the same amplitude of the solution is obtained
230 by increasing the damping coefficient to 1.2. For each dataset, these values should be identified individually using a variation of trials. The first hint for finding the damping weights is considering the evolution of RMS residuals contingent on iterations. When damping is not sufficient, the amplitude of the solution becomes too strong. As a result, deviations of rays with respect to the previous iteration are too strong. In this case, tracing in the next iteration might
235 lead to a non-improved solution. On the other hand, over-damping might provide a too large final RMS. The role of damping parameters is illustrated in the next section. An alternative method for determining the optimal values of damping parameters is synthetic modeling.

The velocity anomalies obtained after inversion are re-computed in a regular grid and added to the velocity model obtained during the previous iteration. Regular representation of the
240 velocity field is more convenient for performing the ray tracing in the next iteration.

3. Example of data processing

3.1. Observed data inversion.

In order to avoid unrealistic synthetic data, the tomographic inversion is applied to two
245 active seismic refraction lines acquired in 1999 in the Musicians Seamount Province ([Figure S1](#)). 13 IFM-GEOMAR ocean bottom hydrophones (OBH) ([Flueh and Bialas, 1996](#)) were deployed along the 180 km long SO142-Line 02, which crosses the Italian Ridge, expressed by an approximately 30 km wide and 3 km high bathymetric elevation. SO 142-Line 04 is 220 km long and covered with 12 OBH. It crosses the Bach Ridge and covers a number of smaller and larger
250 seamounts. The mean instrument spacing along both profiles is approximately 4 km. Two Bolt air guns with a total volume of 64 l served as the seismic source with a shot interval of 60 s and an approximate shot spacing of 120 m at a speed of 4 kt. As is common for oceanic crustal structure investigations, the uniform tectonic structure of the study area yields an excellent data quality, with phases recorded to offsets commonly exceeding 120 km and a high signal-to-noise
255 ratio ([Figure 3](#)). Only in the central part of line 4, some stations display a lower signal-to-noise ratio attenuating phase coherency beyond 50–70 km offset. The oceanic crustal and upper mantle structure of the study area is fairly uniform, especially away from the volcanic edifices. The bathymetric elevations caused by the seamounts produce pronounced variations in apparent velocities. The generally smooth interval velocity distribution along the profiles, however,
260 results in clearly differentiated upper and lower crustal refractions (Puc and Plc) as well as

mantle refraction phases (Pn), which cover the entire shot-receiver offset range on most stations. The upper crustal refraction (Puc) extends to offsets of about 25 km on most record sections, where it merges into the lower crustal arrival (Plc) of gradually increasing velocities (Figure 3). The mantle refraction Pn appears between 50-60 km offset on both profiles, reaching maximum offsets of 140 km.

The observed travel times of the first arrivals of the two profiles are shown by black dots in Figure 4. The data and picking quality are optimal for testing the new algorithm, with a conservatively estimated picking accuracy of 0.03 s at near offsets and 0.12 s at the far offset traces. In total there are more than 20 000 picks for each profile. We did not take into consideration rays of less than 5 km offset between the bounce point and the receiver, because this offset range does not contain any information about the deep interior. After rejecting these rays, the number of rays has reduced to 18716.

Due to the high data density of the study, it is feasible to only use a subset of the data to optimize the calculation speed without loss of the resulting resolution. Figure 5 presents the inversion result based on three datasets with the entire data amount, 1/3 and 1/10. The smoothing and the amplitude coefficients for each of these cases were estimated in several trials. Final values of damping parameters for smoothing (S_m) and amplitude (A_m) ($S_m=8$, $A_m=22$ for the entire dataset, $S_m=5$, $A_m=15$ for the 1/3 dataset and $S_m=3$, $A_m=10$ for the 1/10 dataset) provide stable solutions and similar amplitudes of anomalies. One can see that the results based on the 1/3 and 1/1 datasets are identical. The model based on the 1/10 dataset is slightly smoother. However, it is probable that this difference could disappear if we carefully adjusted the smoothing and amplitude coefficients. This test shows that increasing the amount of data beyond a certain threshold does not always lead to a resolution enhancement. For the main tomographic results presented in Figures 7 and 8 we used 1/3 of the entire data amount (6237 picks), while for searching the optimal parameters and most realistic synthetic model we used the 1/10 dataset that facilitated performing a lot of different trials.

The starting model was parameterized as a 1D velocity model. We defined seismic velocities at distinct depth levels and presumed constant velocity gradients between these levels. In most trials we defined four levels, and only two of them are within the depth range of the study area. Adjusting the 1D model is conducted manually by performing only the first iteration and comparing the RMS of the residuals. For some of the 1D models, we performed a full inversion consisting of 9 iterations. The optimum reference models obtained in this way for the Profiles 02 and 04 are presented in Table 1.

295

Table 1. Starting 1D velocity models used for Profiles 02 and 04

| Profile 02 | | Profile 04 | |
|------------|---------|------------|---------|
| Z, km | V, km/s | Z, km | V, km/s |
| 2 | 3.8 | 2 | 3.7 |
| 6 | 5.7 | 6 | 5.6 |
| 11 | 7.5 | 11 | 7.6 |
| 20 | 7.9 | 20 | 8.0 |

We performed several inversions for each profile using different reference models and various values for the smoothing and amplitude parameters. Decreasing values of these parameters causes stronger sharpness and larger amplitudes of the solution, respectively. The purpose of various trials with different parameters was to determine the optimal values of the parameters, which were evaluated based on values of the RMS reduction curves (Figure 6). If the inversion was not sufficiently damped (too small values of smoothing (Sm) and amplitude (Am)), the next iterations did not provide any improvement of the data RMS with respect to the previous one. This corresponds to a non-stable solution. In case of over-damping during the inversion, the final velocity model was too smooth and did not provide minimal values of the final RMS. Owing to the fast calculation speed provided by the code and using the 1/10 data subset, we were able to inspect dozens of different parameter sets that allowed us to find the optimal solution.

It should be noted that we first used data of Profile 02 as input and thus conducted more trials for this dataset. For Profile 04, assuming similar data characteristics, we used the information obtained for Profile 02 and conducted less trials.

The upper row in Figure 7 presents the result of the data inversion for Profile 02. A positive velocity anomaly is recognized inside the seamount edifice, indicative of an extrusive magmatic origin on top of pre-existing oceanic crust (Kopp et al., 2003). At the depth of 11 km we observe a low velocity anomaly, which shifts the contour line of 7.4 km/s from 10 km to approximately 12 km. It can be suggested that this variation is related to crustal thickening and a downbending of the Moho depth. A similar velocity pattern is observed along Profile 04 (upper row in Figure 8). Travel times of the derived velocity models after inversion of Profiles 02 and 04 are shown in Figure 4 with red dots.

3.2. Combined forward and inverse modeling.

Grid-based inversions generally seek a smooth solution to fit the observed travel times, failing to resolve sharp velocity contrasts. As was stated in the introduction, continuous velocity fields derived from tomographic inversion only represent a crude approximation to the natural

325 velocity distribution, which originates from petrophysical material changes and distinct layer boundaries. In nature the dominant velocity changes are related to first-order velocity changes at petrophysical interfaces. We thus propose a new approach, which enables us to determine the most probable and realistic velocity model based on consequent performing forward and inverse modeling.

330 The code is designed to enable the user to define complicated synthetic models. Two examples of such models are presented in the middle rows of **Figures 7 and 8**. The velocity distribution is defined in areas separated by layer boundaries. Inside each area, a velocity gradient or constant velocity value may be specified. There is also an option for assigning inclined gradients. Furthermore, inside each velocity zone we can designate velocity anomalies
335 with respect to the basic velocity distribution. The shapes of the anomalies are defined by polygons.

The aim of the modeling is to establish a synthetic model, which after performing the forward and inverse modeling process yields a similar velocity distribution as after the inversion of the observed data. The inversion parameters in both cases should be identical. Finding the best
340 model is executed by a trial-and-error method (**Figure S4**). Although tuning of the model is rather time consuming, it is more stable and unique than in the case of classical forward modeling. Indeed, increasing the velocity or lowering the interface in one part of the synthetic model causes a velocity low in the resulting tomographic reconstruction of the same portion of the model.

345 For each profile we tested 12 different synthetic models. Selection of the best model was based on different criteria. The first criterion is the misfit between the observed travel times and the computed travel times during forward modeling in the synthetic model. The values of RMS of observed and synthetic travel time differences, $\|t_{\text{obs}} - t_{\text{synth}}\|$, of 12 different models for each profile are presented in **Table 2**. The second criterion is based on the difference between the
350 velocity models obtained after the final inversion iteration for the observed data and the synthetic data, respectively. This value, which is indicated in **Table 2** as $\|dv_{\text{real}} - dv_{\text{synth}}\|$, is computed on a regular grid for nodes where the solution exists. Analysis of these values in **Table 2** shows that their respective minima do not always coincide for the same model. For example, for Profile 04, the minimal time misfit is observed for Model 4, while the minimal model difference is observed
355 for Model 2. In our opinion, for selecting the best model, the second criterion is more preferable. This is confirmed by visual analysis of the resulting maps (**Figures 7 and 8**), as well as by the similarity of the variance reduction curves (**Figure S6**).

360

Table 2. Values of time and model misfit in different synthetic models. $\|t_{\text{obs}}-t_{\text{synth}}\|$ indicates the RMS between the observed travel times and computed travel times in the synthetic model. $\|dv_{\text{real}}-dv_{\text{synth}}\|$ is the difference between the resulting velocities after 9 iterations of real and synthetic data inversions. Resulting images for the preferred models are presented in **Figures 7 and 8**.

| Profile 02 | | | Profile 04 | | |
|-------------|---------------------------------------|--|-------------|---------------------------------------|--|
| Syn. model: | $\ t_{\text{obs}}-t_{\text{synth}}\ $ | $\ dv_{\text{real}}-dv_{\text{synth}}\ $ | Syn. model: | $\ t_{\text{obs}}-t_{\text{synth}}\ $ | $\ dv_{\text{real}}-dv_{\text{synth}}\ $ |
| 1 | 0.1408 | 0.1841 | 1 | 0.0898 | 0.1783 |
| 2 | 0.0811 | 0.1600 | 2 (pref.) | 0.0612 | 0.0755 |
| 3 | 0.0716 | 0.1488 | 3 | 0.0558 | 0.0988 |
| 4 | 0.0843 | 0.1288 | 4 | 0.0542 | 0.0945 |
| 5 | 0.0666 | 0.1108 | 5 | 0.0651 | 0.1132 |
| 6 | 0.0650 | 0.1119 | 6 | 0.0677 | 0.0936 |
| 7 | 0.0742 | 0.1170 | 7 | 0.0567 | 0.0867 |
| 8 | 0.0733 | 0.1187 | 8 | 0.0797 | 0.0811 |
| 9 | 0.0615 | 0.1027 | 9 | 0.0819 | 0.1182 |
| 10 | 0.0575 | 0.0986 | 10 | 0.0726 | 0.1146 |
| 11 (pref.) | 0.0455 | 0.0877 | 11 | 0.0703 | 0.1128 |
| 12 | 0.0489 | 0.1072 | 12 | 0.0835 | 0.1203 |

365

The model for Profile 02 (**Figure 7**, middle row) consists of three layers separated by a mid-crustal interface and the Moho. In the upper crust, we define a strong velocity gradient of 5.6-6.9 km/s for the depth interval of 6-9 km. In the lower crust, a decreased velocity gradient of 6.9-7.0 km/s for the depth interval of 9-13 km is applied. Beneath the Moho we fix the velocity gradient of 7.85 - 8 km/s for the depth interval of 12 - 15 km. Along the central portion of the profile beneath the seamount, the Moho depth increases from 11 km to ~13.5 km. Inside the seamount edifice, we define a channel of 2-3 km thickness displaying a +18% velocity increase. We tested different values for the channel thickness and amplitudes and found that this configuration provides the most similar reconstruction model (**Figure S4**). To the north of the channel, we specify another positive anomaly of 8% deviation. On the flanks of the seamount we introduce a low velocity anomaly of -12% amplitude.

The model for the Profile 04 (**Figure 8**, middle row) shows a comparable structure. A planar interface separates the upper and lower crust, while the Moho interface shows a more complicated shape than on Profile 02. Similarly, as for Profile 02, in the upper crust, we define a strong velocity gradient of 4.8-6.8 km/s for the depth interval of 4-8 km. In the lower crust the velocity gradient is 6.8-7.0 km/s for the depth interval of 8-13 km. Beneath the Moho we fix the velocity gradient of 7.85 - 8 km/s for the depth interval of 12 - 15 km. Inside the seamount, we define a high velocity anomaly of about 15 km width and an amplitude of +7% - 9%. To the

385

north of this pattern, we define two additional velocity anomalies of +6% and +4% amplitude, respectively. On the flanks of the seamount, we specify sediment velocities with anomalies of – 17% and -20% amplitude.

In both these cases we obtained a good correlation of the inversion results for the
390 observed data and the synthetic data. The travel times corresponding to the synthetic models are shown in [Figure 4](#) with blue dots.

The velocity distribution gained from the tomographic inversion reveals the general tectonic structure of the VERs and supports earlier investigations using tomographic inversion
395 ([Kopp et al., 2003](#)). Crustal thickening along both profiles mainly occurs in oceanic layer 2, which is interpreted as an indication for the extrusive character of the volcanism forming the seamounts and ridges. Top loading of the volcanoes results in a flexural structure of the oceanic crust on both profiles, causing a downbending of the Moho underneath the central volcano. The fine-scale anatomy, however, is only disclosed from the combination of tomographic forward
400 and inverse modeling, e.g. the high-velocity channel discernable in the model for Profile 02, which extends from the lower crust into the seamount edifice ([Figure 7](#), middle row). This feature may possibly be caused by secondary intrusive processes, which though they had been suggested by [Kopp et al. \(2003\)](#) could not be resolved from tomographic inversion alone. Intrusive processes may also be the cause for the broader velocity anomaly along Profile 04. The
405 synthetic model for this profile also includes two smaller-scale anomalies whose origin remains enigmatic. These fluctuations may possibly be linked with the presence of a number of smaller volcanoes adjacent to the ridge. The low velocity anomalies on the flanks of the central volcano of Profile 02 and Profile 04 represent the filled moat structure caused by the downbending of the oceanic crust ([Kopp et al., 2003](#)).

410 Lastly, the role of non-uniqueness needs to be addressed. Indeed the same reconstructed anomalies can either be due to velocity anomalies, or due to interface variations. For example, along Profile 02, the low velocity anomaly at 11 km depth derived in the observed data result is reproduced by a Moho decrease from 11 km down to 13.5 km depth in the synthetic model. The same low velocity anomaly in the reconstruction model could be obtained applying a smaller
415 Moho deviation (e.g., down to 12 km depth) and a coeval greater velocity step at the Moho. However, we cannot significantly change the velocity underneath the Moho because long rays are very sensitive to this value, and its change would cause increasing residuals for such rays. Thus the contrast may be increased by a velocity decrease at the base of the crust. However, our options are limited as well here, because the value of 6.8 km/s at 8 km depth is fixed to model
420 the travel times of shallow rays. Decreasing the velocity value in the crust at 13 km depth would

cause a negative velocity gradient, which is not probable. This discussion is given to show that although the theoretical problem of non-uniqueness exists in forward/inverse modeling, in practice we do not have much freedom in creating geologically reasonable models that satisfy the data. To reduce the ambiguity related to non-uniqueness it is fruitful to incorporate a-priory information if available.

3.3. Checkerboard Resolution Test

Besides the reconstruction of realistic shapes of anomalies described in the previous section, the *PROFIT* code also allows conducting a variety of different synthetic tests. In this section we present the results of the traditional checkerboard test. The initial model for this test (upper row of [Figure 9](#)) is represented by alternated positive and negative anomalies of $\pm 3\%$ amplitude. Horizontal and vertical sizes of each block are 10 km by 2 km. The travel times were computed using a 2D bending ray tracer. It should be noted that rays computed in this way tend to travel through high velocity anomalies. Therefore the reconstruction in the first iteration is strongly biased to the positive value. After several iterations the solution becomes more balanced regarding the amplitudes of positive and negative anomalies. Iteration 9 shows a fairly stable reconstruction of most patterns in the area beneath the stations. This test documents the importance of using a non-linear iterative approach in tomographic inversions, since the ray paths in the first and the final iterations differ significantly. The capacity of the algorithm to resolve different sizes of patterns in different parts of the study area is illustrated by a series of checkerboard tests with different sizes of patterns presented in [Figure S7](#). It can be seen that even the patterns of 3 km width and 1 km depth can be resolved in the center of the profile in the uppermost part. The larger anomalies are resolved in larger areas.

4. Conclusions

Using 2D-wide angle seismic profiles across the Musicians Seamounts, we demonstrated the capability of combined tomographic forward and inverse modeling. We developed a new code, which minimizes computation time by applying a new algorithm of the bending method of ray tracing. In contrast to the graph methods of pseudo bending commonly used, our bending method does not require using any grid. It allows any velocity parameterization (with cells or nodes, with polygons or layers, with some analytical laws etc). As a result, it provides more accurate solutions in significantly shorter calculation time.

Our new approach uses the output model of the observed data tomography to construct a geologically reasonable synthetic model of the study area. This procedure is beneficial to the

455 geologic-tectonic interpretation in that it provides a structural model in addition to the
continuous velocity field created by the tomography.

The tomography inversion supports the dominance of extrusive volcanism in the
Musicians Seamount Province, causing a thickening of oceanic layer 2. In addition, from the
structural forward modeling, we were able to identify secondary intrusive processes, which
460 added to the evolution of the VERs. Whereas the velocity-depth distribution derived from the
tomographic inversion provides a substantiated image of the dominating tectonic processes, the
detailed anatomy of the volcanic ridges could only be resolved by the combined approach of
tomographic forward and inverse modeling. This new procedure was used to obtain a realistic
structural model, which satisfies the observed travel times.

465 The executable version of the PROFIT code is available online at [www.ivan-
art.com/science/PROFIT](http://www.ivan-art.com/science/PROFIT). The detailed description of the code can be found in the same location.
The source codes (in Fortran 90) are freely provided to any interested person by Ivan Koulakov
through email communication. Further development of the *PROFIT* code is planned. In
particular, we are working on including reflected and head waves in addition to the first arrivals.
470 These data will be used for simultaneous inversion of velocity structures and geometry of
interfaces.

Acknowledgements

The refraction data were acquired by RV SONNE in the 1998 HULA experiment
475 (supported by the German Ministry of Finance and Education BMBF). Ivan Koulakov was
partially supported by RFBR (grant #08-05-00276). We thank C. Kopp and A. Shulgin for
fruitful discussions on seismic tomography.

References

- 480
- Flueh, E. R., and J. Bialas, A digital, high data capacity ocean bottom recorder for seismic
investigations, *Int.Underwater Syst.Design*, 18(3), 18-20, 1996.
- Hobro, J. W. D., S. C. Singh and T. A. Minshull (2003) Three-dimensional tomographic
inversion of combined reflection and refraction seismic travelttime data, *Geophys. J. Int.*,
485 152, 1, 79-93, doi:10.1046/j.1365-246x.2003.01822.x
- Hole, J. A. (1992) Nonlinear High-Resolution Three-Dimensional Seismic Travel Time
Tomography, *J. Geophys. Res.*, 97, B5, 6553-6562.
- Kopp, H., C. Kopp, J. Phipps Morgan, E. R. Flueh, W. Weinrebe, and W. J. Morgan (2003),

- 490 Fossil hot spot-ridge interaction in the Musicians Seamount Province: Geophysical
investigations of hot spot volcanism at volcanic elongated ridges, *J. Geophys. Res.*,
108(B3), 2160, doi:10.1029/2002JB002015.
- Korenaga, J., W. S. Holbrook, G. M. Kent, P. B. Kelemen, R. S. Detrick, H.-C. Larsen, J. R.
Hopper and T. Dahl-Jensen (2000) Crustal structure of the southeast Greenland margin
from joint refraction and reflection seismic tomography, *J. Geophys. Res.*, 105, B9,
495 21,591-21,614.
- Koulakov, I., M. Bohm, G. Asch, B.-G. Lühr, A. Manzanares, K.S. Brotopuspito, Pak Fauzi, M.
A. Purbawinata, N.T. Puspito, A. Ratdomopurbo, H. Kopp, W. Rabbel, E. Shevkunova
(2007), P and S velocity structure of the crust and the upper mantle beneath central Java
from local tomography inversion, *J. Geophys. Res.*, 112, B08310,
500 doi:10.1029/2006JB004712.
- Koulakov, I., (2008), LOTOS code for local earthquake tomographic inversion. Benchmarks for
testing tomographic algorithms, *Bull. Seism. Soc. Am.*, in review, 2008.
- Luetgert, J.H., 1992. MacRay - Interactive two-dimensional seismic raytracing for the
Macintosh. USGS, Open File Report 92-356.
- 505 Paige, C.C., and M.A. Saunders, (1982), LSQR: An algorithm for sparse linear equations and
sparse least squares, *ACM Trans. Math. Soft.*, 8, 43-71.
- Thurber, C. (1993), Local earthquake tomography: Velocities and V_p/V_s – theory, in *Seismic
Tomography, Theory and Practice*, edited by H. Iyer and K. Hirahara, CRC Press, Boca
Raton, Fla. pp. 563– 583.
- 510 Um, J., and Thurber, (1987), A fast algorithm for two-point seismic ray tracing, *Bull. Seism. Soc.
Am.*, 77, 972-986.
- Van der Sluis, A., and H.A. van der Vorst, (1987), Numerical solution of large, sparse linear
algebraic systems arising from tomographic problems, in: *Seismic tomography*, edited by
G. Nolet, pp. 49-83, Reidel, Dordrecht,
- 515 Zelt, C. A. and R. B. Smith (1992) Seismic travelttime inversion for 2-D crustal velocity
structure, *Geophys. J. Int.*, 108, 16-34.
- Zelt, C. A., and P. J. Barton (1998) Three-dimensional seismic refraction tomography: A
comparison of two methods applied to data from the Faeroe Basin, *J. Geophys. Res.*, 103,
7187-7210.

520

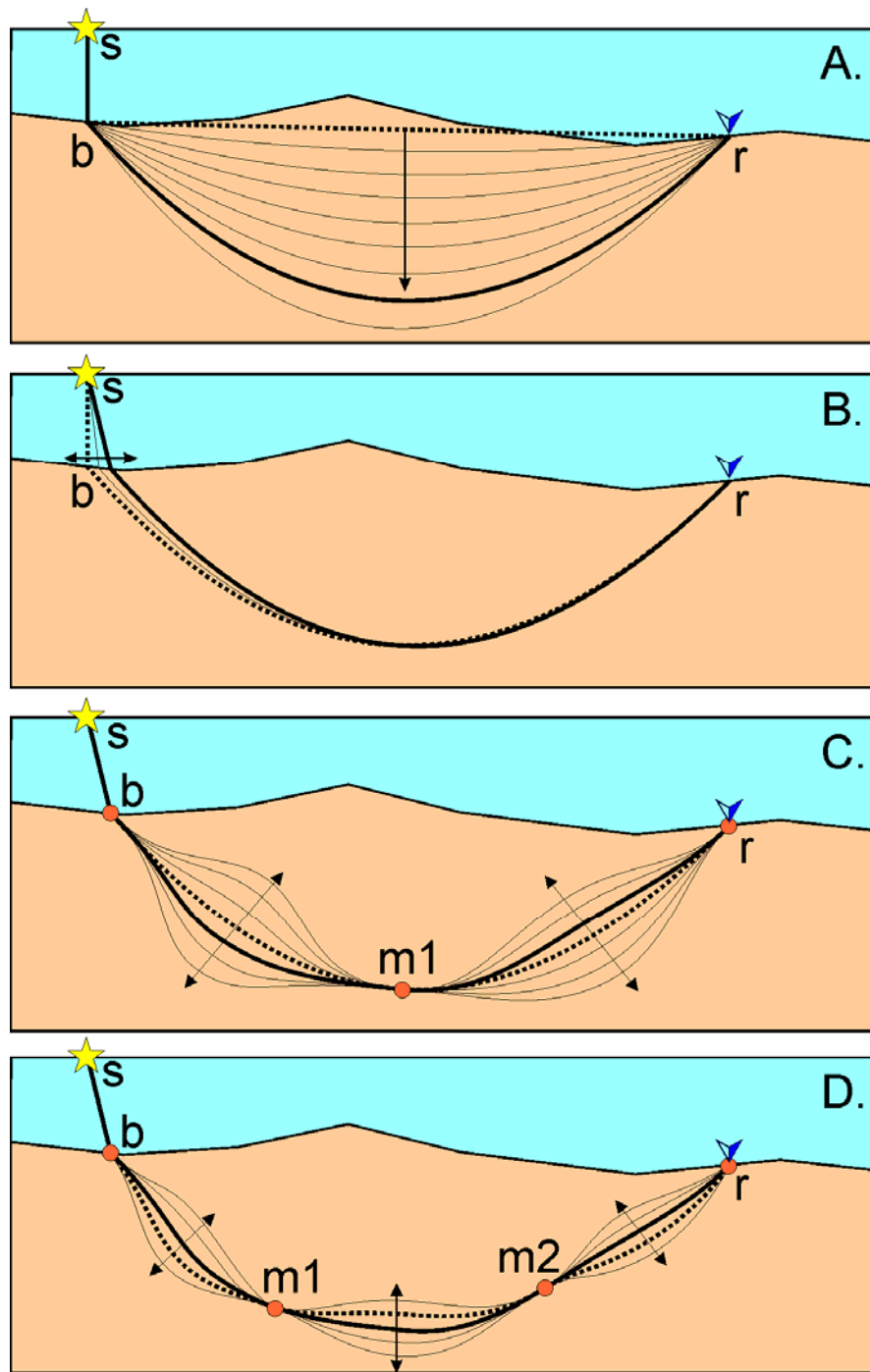


Figure 1. Sketch for explaining the principle of our version of the bending algorithm (please refer to the text for details).

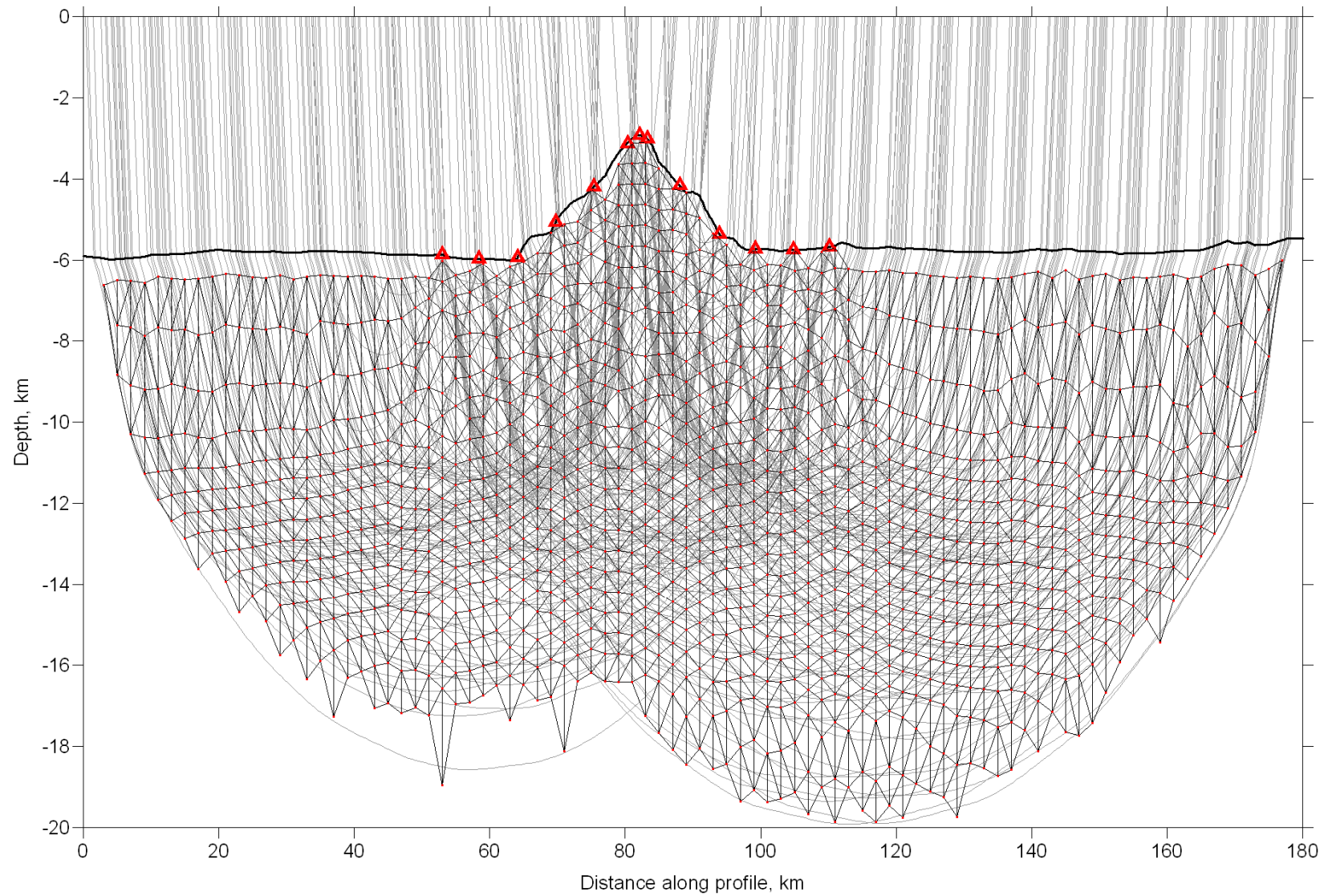


Figure 2. Ray paths and parameterization grid. The rays (grey lines) correspond to real observations along Profile 02 traced in the starting 1D velocity model. Thick black line traces the seafloor; red triangles indicate locations of ocean bottom stations. Parameterization nodes are shown with red dots. Segments indicate links between neighboring nodes, which are used for smoothing during the inversion.

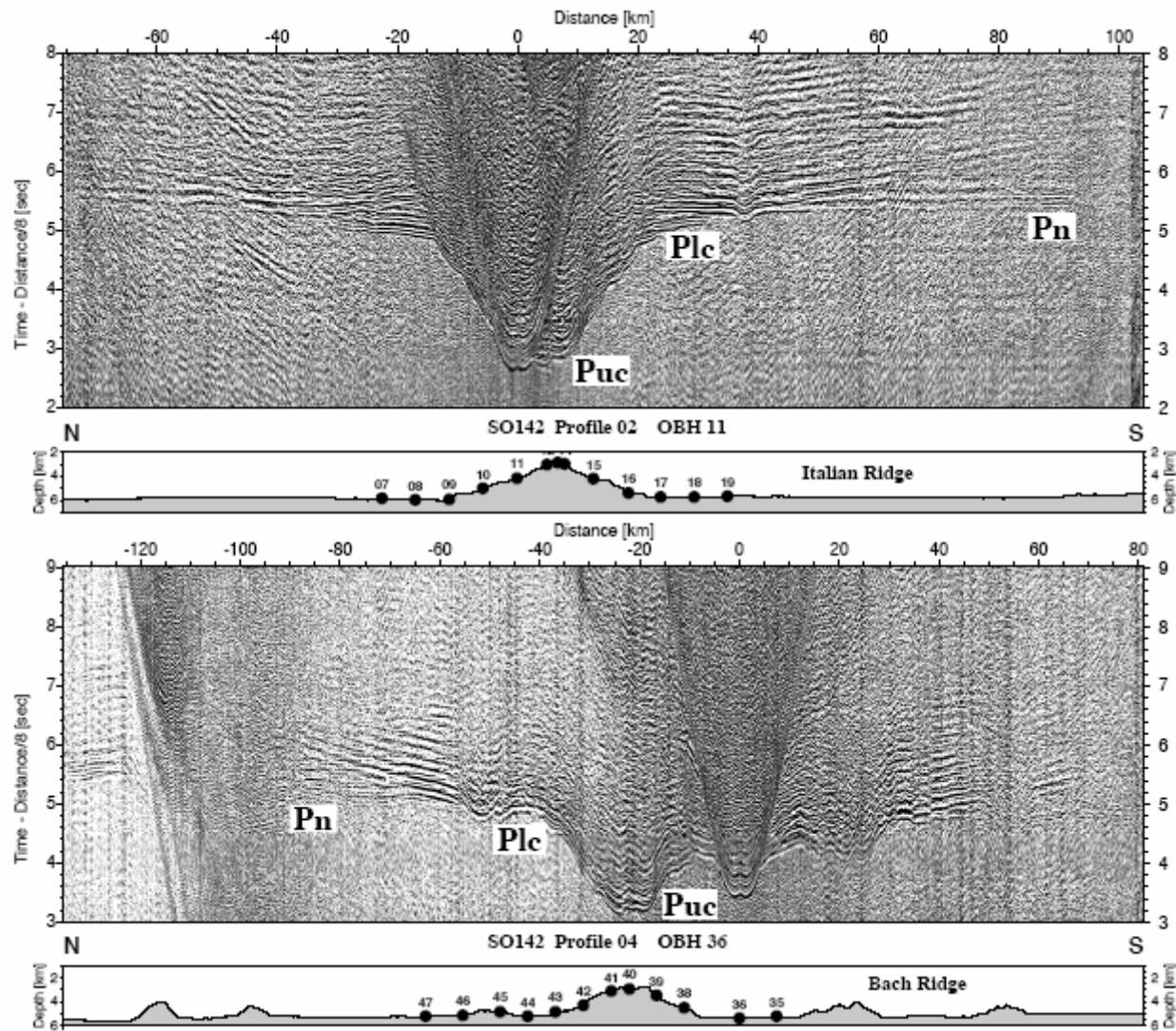


Figure 3. Seismic wide-angle sections for OBH 11 of Profile 02 and OBH 36 of Profile 04, respectively. Clear phases from the upper crust (Puc), lower crust (Plc) and mantle (Pn) are recognized to offsets of more than 100 km on a number of stations. Seafloor topography causes strong apparent velocities.

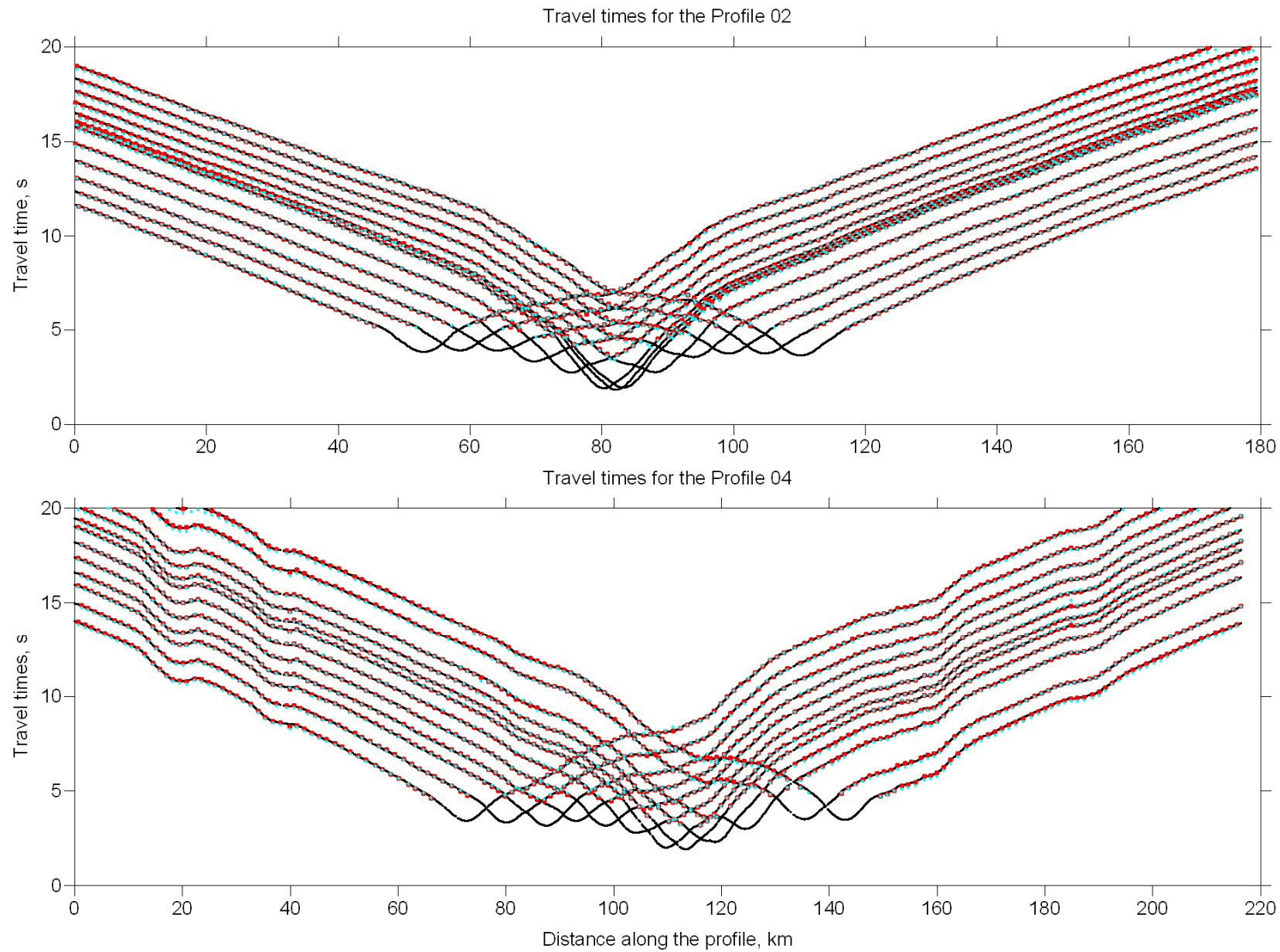


Figure 4. Travel times for Profiles 02 and 04, respectively. Black dots present the observed travel times. Blue dots are the travel times in the synthetic model (middle row in [Figures 7-8](#)). Red dots are the travel times in the resulting model after inversion of the observed data (upper row in [Figures 7-8](#)).

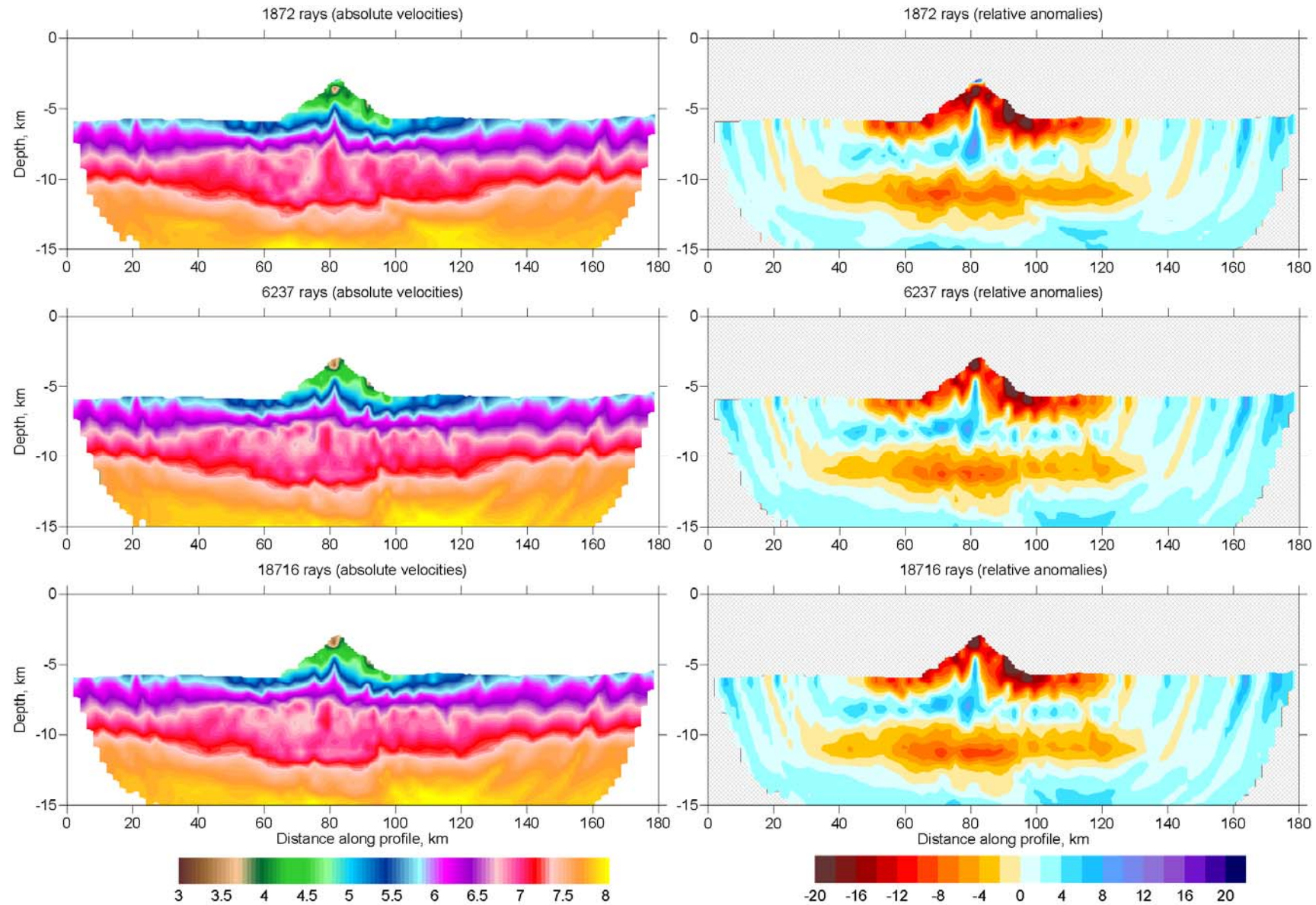


Figure 5. Inversion results based on 1/10 and 1/3 data subsets (upper and middle row, respectively) and the entire data set (bottom row). Numbers of rays for each case are indicated. In the left column, the models are presented in absolute velocity values. The right column presents relative perturbations with respect to the 1D starting model, which is identical for all three cases.

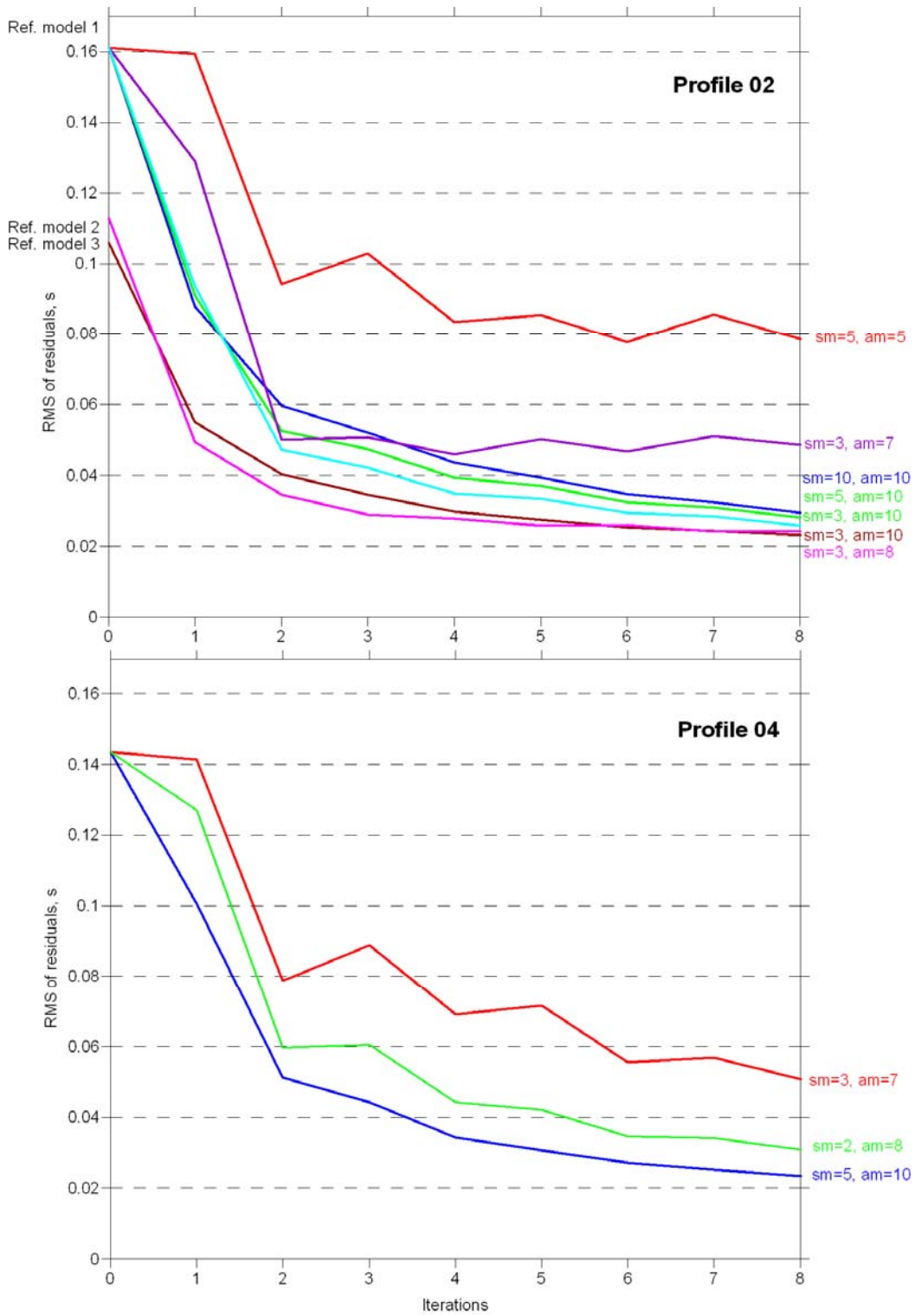


Figure 6. Values of RMS of residuals after eight iterations for two datasets (Profile 02 and 04). The curves correspond to different values of weights of amplitude (Am) and smoothing (Sm). For Profile 02, we considered three different reference models.

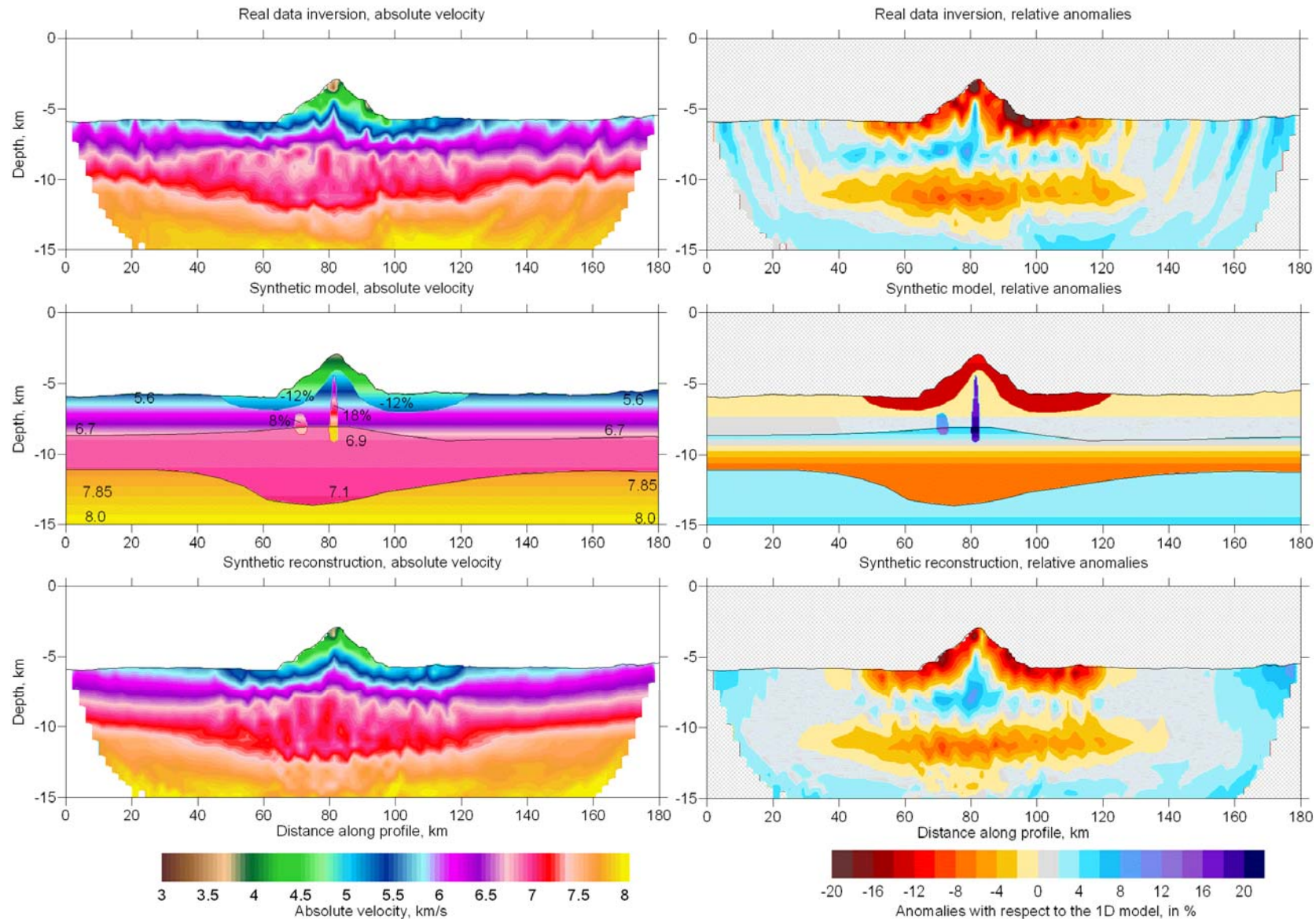


Figure 7. Results of real data inversion and synthetic reconstruction for Profile 02. In left column, the models are presented in absolute velocity values. The right column presents relative perturbations with respect to the 1D starting model, which is identical for all three cases. Results of real data inversion are shown in the upper row. Synthetic model, which was constructed after several trials, is shown in middle row. Values of velocities are indicated in km/s. The reconstruction result after forward modeling in the synthetic model and inversion with the same parameters as in the real case is displayed in the bottom row.

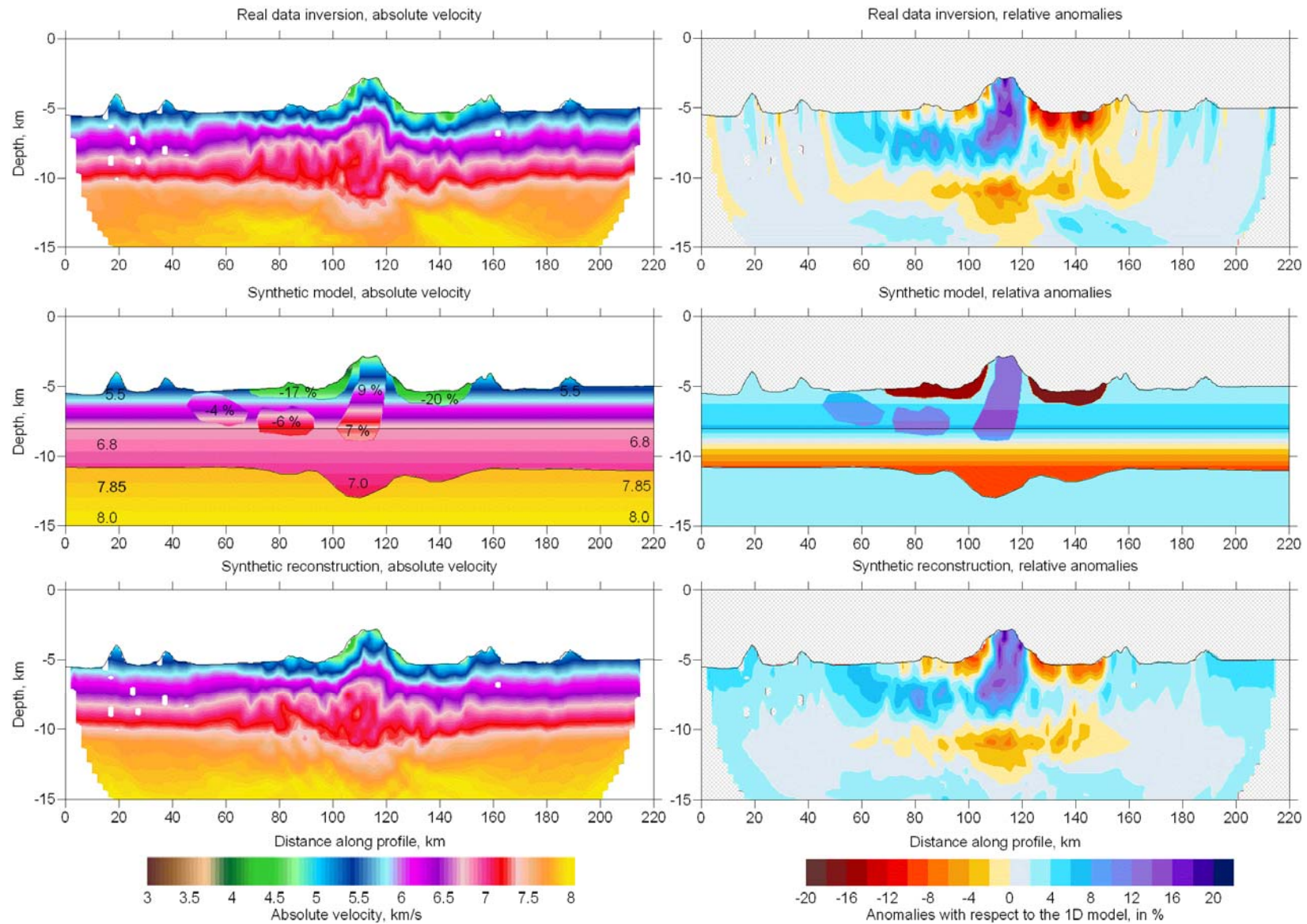


Figure 8. Results of real data inversion and synthetic reconstruction for Profile 04. Please refer to Figure 7 for display information.

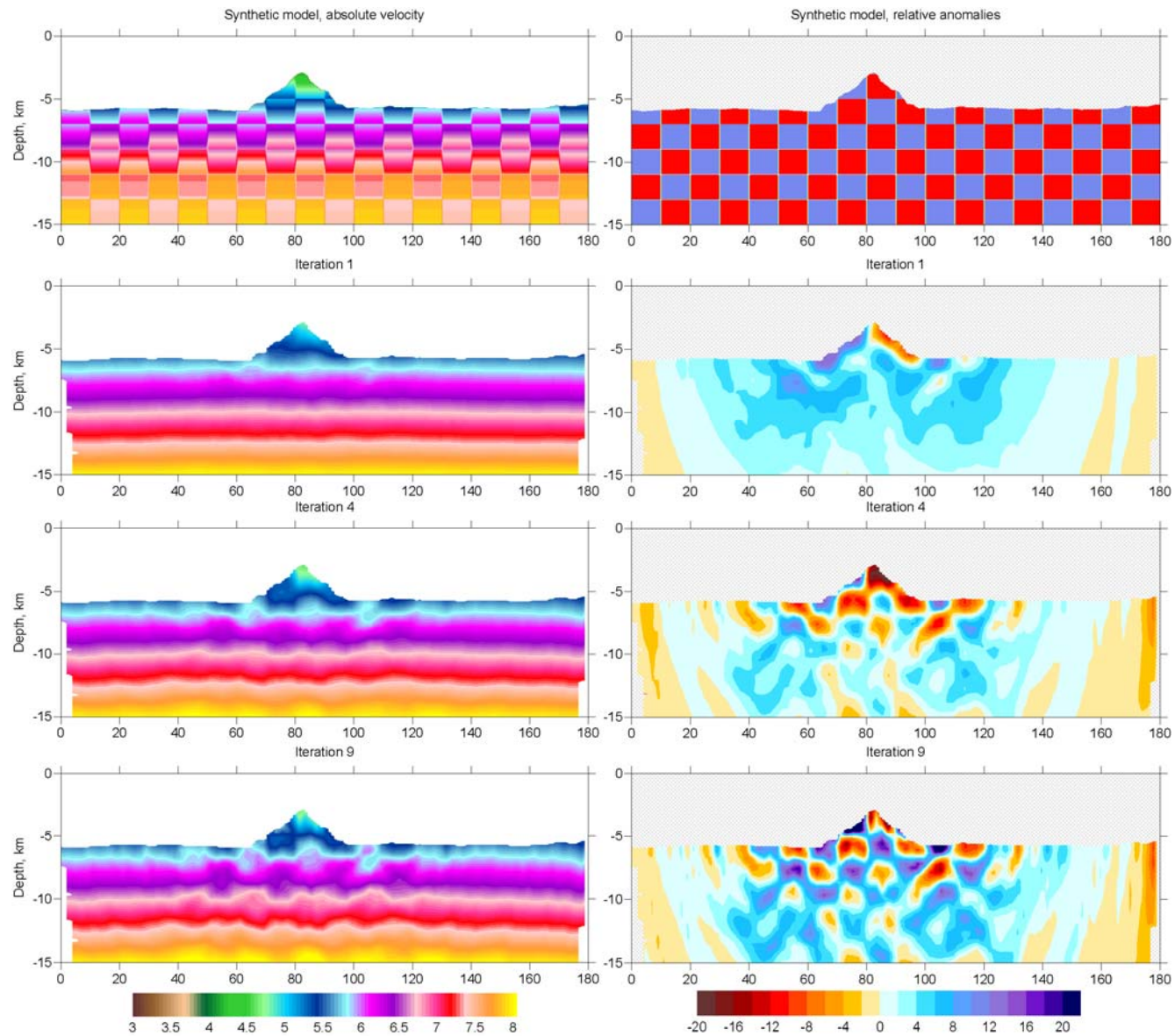


Figure 9: Results of the checkerboard resolution test with anomalies of 10 km and 2 km of horizontal and vertical sizes, respectively, and $\pm 3\%$ amplitude. Left and right columns represent absolute velocity and relative anomalies (in % with respect to 1D model), respectively. Upper row shows the synthetic model. Lower rows present the reconstruction results in iterations 1, 4, and 9.